Ionic Interaction Effects on the Structure and Dynamics of Orthoborate Ionic Materials

CRYSTAL GROWTH & DESIGN

pubs.acs.org/crystal

Article

Ionic Interaction Effects on the Structure and Dynamics of Orthoborate Ionic Materials

Yanqi Xu, Anders Reinholdt, Oleg N. Antzutkin, Maria Forsyth, Patrik Johansson,* and Faiz Ullah Shah*

Cite This: *Cryst. Growth Des.* 2024, 24, 8989−8998

Read Online

ACCESS | Metrics & More | Article Recommendations | Supporting Information

ABSTRACT: A series of orthoborate-based ionic materials of bis(glycolato)borate ([BGB]) and bis(ethylene-1,2-dioxy)borate anions ([BEDB]) coupled with tetrabutylphosphonium ([P_{4444}]) and tetrabutylammonium ([N_{4444}]) cations have been synthesized, and their physicochemical properties are characterized. The ionic materials based on the most popular orthoborate anion, bis(oxalato)borate anion ([BOB]), which contains four carbonyl groups, are all liquid at ambient temperature, while the bis(glycolato)borate ([BGB]) anion, with two carbonyl groups, and the bis(ethylene-1,2-dioxy)borate ([BEDB]) anion, without carbonyl groups, render solids at ambient temperature. The ionic materials based on the [BGB] anion display the highest decomposition temperatures, and those based on the BEDB anion are the lowest. The [P_{4444}][BGB], [P_{4444}][BEDB], and [N_{4444}][BEDB] salts feature significantly wider plastic phase I temperature ranges than their analogues. FTIR spectroscopy, multinuclear (^{15}N, ^{31}P, ^{13}C, and ^{11}B) solid-state NMR spectroscopy, and single-crystal X-ray diffraction were all used to unveil the ionic interactions and structural features, which display weaker ionic interactions for [BEDB] compared to [BGB] when bearing the same cation and present relatively higher crystallinity of [P_{4444}][BGB] among the ionic materials.

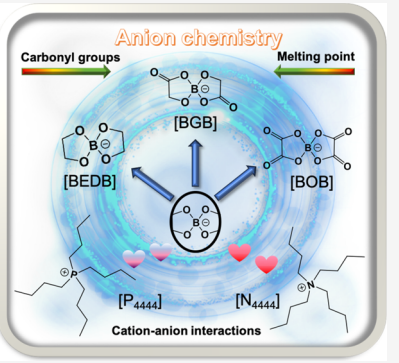

INTRODUCTION

Boron compounds and boron-based salts have promising properties suited for many application areas such as lubrication,[1] pharmaceutics,[2] electronics,[3] and energy storage.[4] As for medicinal use, the U.S. FDA in 2003 approved the first proteasome inhibitor bortezomib, for treating multiple myeloma that contains boron[5] (PS-341 or Velcade). Boron-containing polymers can provide advanced features including lightweight, high melting point, flexibility, etc. for electronic applications,[3] and in the context of energy storage applications, boron compounds provide distinctive benefits for enhanced performance in battery applications, as various novel anionic boron clusters and boron-containing solid materials have been proposed as components of novel electrolytes, potentially replacing conventional electrolytes.[6−12]

Among solid-state materials for energy applications, organic ionic plastic crystals (OIPCs) have emerged as attractive solid-state electrolytes (SSEs) for lithium-ion batteries (LIBs) and sodium-ion batteries (SIBs) and have been widely studied over the past decade.[13−18] Similar to room-temperature ionic liquids (RTILs), OIPCs possess a combination of highly wanted electrolyte properties including nonvolatility, nonflammability, high thermal stability, high ionic mobility, and structural designability. This makes the OIPCs strong SSE candidates. In addition, the increased disorder and defects present in OIPCs at elevated temperatures provide plasticity and enhanced diffusion, improving the ionic conductivity.[19] This is important and a challenge as in contrast to RTILs that have ionic conductivities in the range from 10^{-4} to 10^{-3} S cm^{-1} at ambient temperature,[20,21] OIPCs still have too low ionic conductivities, for example, battery application.[16]

Most of the reported OIPCs are based on heavily fluorinated anions such as bis(fluorosulfonyl)imide ([FSI]),[22] bis(trifluoromethanesulfonyl)imide ([TFSI]),[23] hexafluorophosphate ([PF_6]$^-$),[24] and tetrafluoroborate ([BF_4]$^-$).[25] By employing a halide-free synthesis route, Kang et al.[26] created OIPCs with the new difluoro(oxalato)borate ([DFOB]) anion coupled with either triethylmethylammonium ([N_{1222}]) or 1-ethyl-1-methylpyrrolidinium ([C_2mpyr]) cations, which showcased combined benefits of good solid electrolyte interphases (SEIs), Al corrosion inhibition, high salt solubility, and nonflammability. Yunis et al.[27] synthesized a series of *N*,*N*-diethylpyrrolidinium ([C_2epyr]) cation-based RTILs and plastic crystals; the RTILs were formed when the cation was combined with fluorosulfonyl(trifluoromethanesulfonyl)imide ([FTFSI]) and dicyanamide ([DCA]) anions, while OIPCs were obtained when coupled to [TFSI], [FSI], [PF_6]$^-$, and [BF_4]$^-$ anions. The OIPCs displayed beneficial thermal and transport properties, and the [C_2epyr][FSI] exhibited an ionic conductivity of 1.9×10^{-5} S cm^{-1} at 30 °C. The ionic conductivity can be further increased by mixing

Received: July 24, 2024
Revised: September 30, 2024
Accepted: September 30, 2024
Published: October 9, 2024

https://doi.org/10.1021/acs.cgd.4c01030
Cryst. Growth Des. 2024, 24, 8989−8998

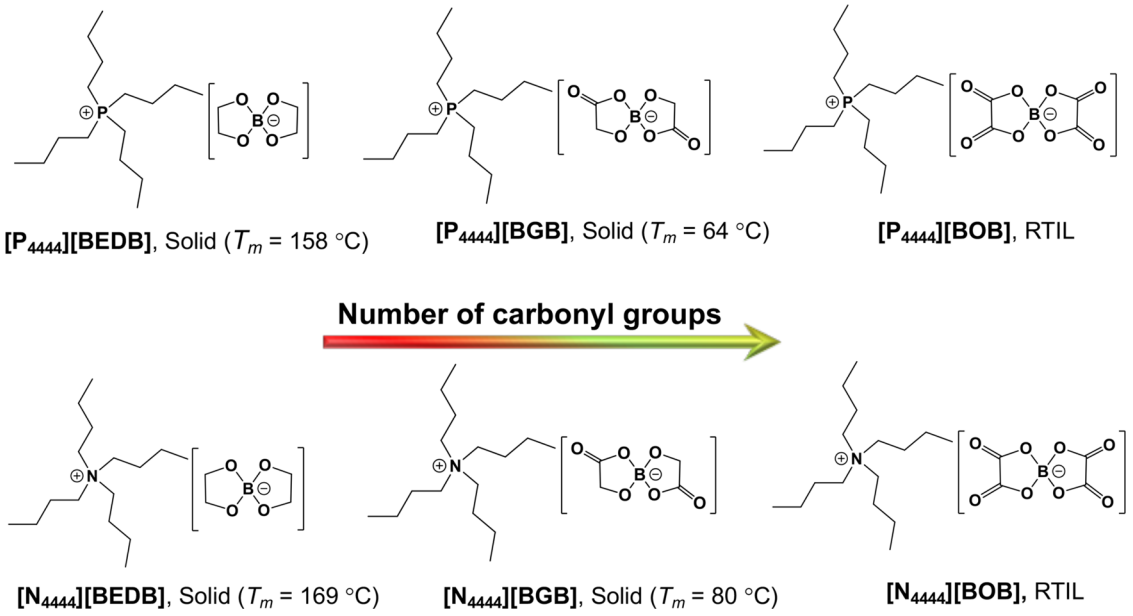

Figure 1. Chemical structures of the synthesized orthoborate ionic materials containing $[P_{4444}]$ and $[N_{4444}]$ cations.

different OIPCs. For example, Abeysooriya et al.[28] showed that $[C_2epyr][FSI]$ and *N*-isopropyl-*N*-methylpyrrolidinium [FSI] ($[C_{(i3)}mpyr][FSI]$) OIPCs in a 1:9 molar ratio reached an ionic conductivity of 1.8×10^{-3} S cm^{-1} at 30 °C. As unveiled by synchrotron XRD analysis, this mixture has increased defect volume and/or rotational disorder, which facilitates ion conduction.

Inspired by the work by Ue et al.,[29] focusing on bis(oxalato)-borate anion ([BOB]) analogues with five-membered orthoborate rings, we aim to create OIPCs and have synthesized a series of new fluorine-free orthoborate-anion-based ionic materials using the bis(glycolato)borate ([BGB]) and bis(ethylene-1,2-dioxy)borate anions ([BEDB]) combined with organic cations, such as tetrabutylphosphonium ($[P_{4444}]$) and tetrabutylammonium ($[N_{4444}]$) and compared with popular bis(oxalato)borate, [BOB]-based counterparts (Figure 1). However, as will be clear from below, not all our solid ionic materials are indeed (classical) OIPCs, and we will outline the underlying reasons. The structures and properties have been systematically investigated using various characterization techniques, with emphasis on the interactions present and with the final aim of verifying/dismissing their promise as battery electrolyte materials.

EXPERIMENTAL SECTION

Synthesis. The synthesis of orthoborate ionic materials was performed keeping in mind the 12 fundamental principles of green chemistry.[30] Briefly, the synthesis involved mixing of boric acid and the corresponding acid using water as the solvent to get the acidic form of the orthoborate, followed by a neutralization reaction with either tetrabutylphosphonium or tetrabutylammonium hydroxide.

[BEDB] Salts. Tetrabutylphosphonium bis(ethylene-1,2-dioxy)-borate ($[P_{4444}][BEDB]$) and tetrabutylammonium bis(ethylene-1,2-dioxy)borate ($[N_{4444}][BEDB]$) salts were prepared using a slightly modified procedure with respect to the previously reported synthesis path.[31] Briefly, 0.02 mol ethylene glycol ($C_2H_6O_2$, Sigma-Aldrich, ≥99%) and 0.01 mol boric acid (H_3BO_3, Sigma-Aldrich, ≥99.5%) were dissolved in 100 mL deionized water (H_2O, 18.25 MΩ cm, Millipore, Merck) and stirred at 60 °C for 3−4 h. Afterward, either 40 wt % tetrabutylphosphonium hydroxide aqueous solution (TCI, 40 wt %) or 40 wt % tetrabutylammonium hydroxide solution (Sigma-Aldrich, 40 wt %) was added to the reaction mixture followed by continuous stirring at 50 °C for 24 h. The water was removed at reduced pressure using a rotary evaporator to obtain the product. The product was washed with a mixture of ethyl acetate (VWR, technical) and hexane (VWR, technical) (1:1 volume ratio). Finally, the traces of solvents were removed using a rotary evaporator, and the product was dried in a vacuum oven at 90 °C for at least 2 days.

$[P_{4444}][BEDB]$. White solid (95% yield). ^{1}H NMR (400.21 MHz, $CDCl_3$) δ 3.74 (s, 8H, $-CH_2-O$), 2.41−2.37 (m, 8H, $-CH_2-P$), 1.53 (s, 16H, $-CH_2-$), 0.99 (t, 12H, $-CH_3$) ppm. ^{13}C NMR (100.64 MHz, $CDCl_3$) δ: 63.71, 24.28, 24.13, 24.06, 18.93, 18.46, 13.71 ppm. ^{11}B NMR (128.40 MHz, $CDCl_3$): 10.99 ppm. ^{31}P NMR (162.01 MHz, $CDCl_3$): 33.10 ppm.

$[N_{4444}][BEDB]$. White solid (89% yield). ^{1}H NMR (400.21 MHz, $CDCl_3$) δ 3.73 (s, 8H, $-CH_2-O$), 3.35−3.31 (m, 8H, $-CH_2-N$), 1.64−1−61 (m, 8H, $-CH_2-$) 1.49−1.40 (m, 8H), 1.01 (t, 12H, $-CH_3$) ppm. ^{13}C NMR (100.64 MHz, $CDCl_3$) δ: 63.86, 58.70, 24.27, 19.91, 13.90 ppm. ^{11}B NMR (128.40 MHz, $CDCl_3$): 10.72 ppm.

[BGB] Salts. Tetrabutylphosphonium bis(glycolato)borate ($[P_{4444}]$-[BGB]) and tetrabutylammonium bis(glycolato)borate ($[N_{4444}]$-[BGB]) were prepared using the previously reported procedure.[29] Briefly, 0.1 mol glycolic acid ($C_2H_4O_3$, Sigma-Aldrich, ≥99%) and 0.05 mol boric acid were dissolved in 100 mL H_2O to form a homogeneous solution. The solution was stirred for 30 min at ambient temperature, followed by the addition of either 40 wt % tetrabutylphosphonium hydroxide solution or 40 wt % tetrabutylammonium hydroxide solution. The reaction mixture was continuously stirred at ambient temperature for 24 h, and then water was removed at reduced pressure using a rotary evaporator. The final product ($[P_{4444}][BGB]$) was purified by washing with ethyl acetate and hexane (1:2 volume ratio). In the case of $[N_{4444}][BGB]$, a mixture of dichloromethane (VWR, technical) and hexane (1:1 volume ratio) was used to wash the product. Traces of solvents were rotary evaporated, and the final product was dried in a vacuum oven at 90 °C for 3 days.

$[P_{4444}][BGB]$. White solid (98% yield). ^{1}H NMR (400.21 MHz, DMSO-d_6) δ 3.92 (s, 4H, $-CH_2-O$), 2.21−2.14 (m, 8H, $-CH_2-P$), 1.47−1.38 (m, 16H, $-CH_2-$), 0.92 (t, 12H, $-CH_3$) ppm. ^{13}C NMR (100.64 MHz, DMSO-d_6) δ: 177.49, 65.55, 24.05, 23.90, 23.25, 23.21, 18.13, 17.66, 13.87 ppm. ^{11}B NMR (128.40 MHz, DMSO-d_6): 11.41 ppm. ^{31}P NMR (162.01 MHz, DMSO-d_6): 33.80 ppm.

$[N_{4444}][BGB]$. White solid (95% yield). ^{1}H NMR (400.21 MHz, DMSO-d_6) δ 3.92 (s, 4H, $-CH_2-O$), 3.18−3.14 (m, 8H, $-CH_2-N$), 1.56 (s, 8H, $-CH_2-$) 1.33−1.28 (m, 8H, $-CH_2-$), 0.93 (t, 12H, $-CH_3$) ppm. ^{13}C NMR (100.64 MHz, DMSO-d_6) δ: 177.49, 65.55,

https://doi.org/10.1021/acs.cgd.4c01030
Cryst. Growth Des. 2024, 24, 8989−8998

58.12, 23.67, 19.81, 14.08 ppm. ^{11}B NMR (128.40 MHz, DMSO-d_6): 11.41 ppm.

[BOB] Salts. Tetrabutylphosphonium bis(oxalato)borate ([P_{4444}][BOB]) and tetrabutylammonium bis(oxalato)borate ([N_{4444}][BOB]) were prepared using the previously reported procedure.[29] Briefly, 0.02 mol of oxalic acid ($C_2H_2O_4$, Sigma-Aldrich) and 0.01 mol of boric acid were dissolved in 100 mL of deionized H_2O to get a clear solution. The solution was stirred at 50 °C for 30 min, followed by addition of either 40 wt % tetrabutylphosphonium hydroxide solution or 40 wt % tetrabutylammonium hydroxide solution. The reaction mixture was stirred at 50 °C for 24 h, and water was removed using a rotary evaporator. The [P_{4444}][BOB] product was washed with ethyl acetate and hexane (1:1 volume ratio) at least 3 times. For [N_{4444}][BOB], a mixture of DCM and hexane (1:1 volume ratio) was used to purify the product. The final product was dried in a vacuum oven at 90 °C for 3 days.

[P_{4444}][BOB]. Light yellow liquid (95% yield). ^{1}H NMR (400.21 MHz, DMSO-d_6) δ 2.22−2.15 (m, 8H, $-CH_2-$P), 1.48−1.40 (m, 16H, $-CH_2-$), 0.92 (t, 12H, $-CH_3$) ppm. ^{13}C NMR (100.64 MHz, DMSO-d_6) δ: 158.75, 24.05, 23.90, 23.26, 23.22, 18.16, 17.68, 13.87 ppm. ^{11}B NMR (128.40 MHz, DMSO-d_6): 7.37 ppm. ^{31}P NMR (162.01 MHz, DMSO-d_6): 33.78 ppm.

[N_{4444}][BOB]. Light yellow liquid (85% yield). ^{1}H NMR (400.21 MHz, $CDCl_3$) δ 3.25−3.21 (m, 8H, $-CH_2-$N), 1.68−1.64 (m, 8H, $-CH_2-$), 1.46−1.40 (m, 8H, $-CH_2-$), 1.01 (t, 12H, $-CH_3$) ppm. ^{13}C NMR (100.64 MHz, $CDCl_3$) δ: 158.97, 59.00, 23.99, 19.79, 13.67 ppm. ^{11}B NMR (128.40 MHz, $CDCl_3$): 7.66 ppm.

NMR Spectroscopy. Solution-state multinuclear (^{1}H, ^{13}C, ^{11}B, and ^{31}P) nuclear magnetic resonance (NMR) spectroscopy was performed using a Bruker Ascend Aeon WB 400 (Bruker BioSpin AG, Fällanden, Switzerland) spectrometer. The working frequencies were 400.21 MHz for ^{1}H, 162.01 MHz for ^{31}P, 128.40 MHz for ^{11}B, and 100.64 MHz for ^{13}C. Samples were dissolved in DMSO-d_6 or $CDCl_3$ and placed either in a 5 or 10 mm standard glass tube. All the solution (^{1}H, ^{13}C, ^{11}B and ^{31}P) NMR spectra are provided in Figures S1 and S21 in the Supporting Information (SI).

Solid-state multinuclear (^{13}C, ^{11}B, ^{31}P, and ^{15}N) magic-angle-spinning (MAS) NMR experiments were carried out using the same spectrometer and either 5 mm (for ^{13}C, ca. 100 mg samples) or 4 mm (for ^{11}B, ^{31}P, and ^{15}N, ca. 40 mg samples) MAS probes with samples (fine white powder) packed in zirconia rotors and spun at 5 or 8 kHz. The working frequencies for ^{13}C, ^{11}B, and ^{31}P were the same as above, and the working frequency for ^{15}N NMR was 40.56 MHz. The NMR spectra were recorded using either the direct-excitation single-pulse experiment with proton decoupling or with cross-polarization (CP) from protons using ramping of the rf-field in the X-channel from 70 to 100% of the maximum amplitude and 2.5/2/1.5 ms contact time for ^{1}H−^{31}P/^{1}H−^{13}C/^{1}H−^{15}N, respectively, and also with proton decoupling. A 93 kHz "Spinal-64" sequence[32] for proton decoupling with rf-pulses in the proton channel was used to average out the dipole−dipole ^{13}C−^{1}H/^{31}P−^{1}H/^{15}N−^{1}H interactions. ^{11}B and ^{31}P NMR spectra were externally referenced using liquid samples of $Et_2O{\cdot}BF_3$ (0 ppm) for ^{11}B and H_3PO_4 (85%, 0 ppm) for ^{31}P. The liquid samples were placed in a small capillary (1 mm diameter) and inserted into an empty 4 mm rotor to minimize the differences in magnetic susceptibility between powder samples and the liquid reference. For ^{13}C and ^{15}N, solid adamantane (38.48 ppm from TMS, $\delta(^{13}C)$ = 0 ppm) and polycrystalline ^{15}N-enriched (98%) $^{15}NH_4Cl$ (0 ppm) were used as external references. All measurements were performed at 293 K, and the NMR spectra were processed using Bruker Topspin 3.5 software. The solid-state (^{13}C, ^{11}B, ^{31}P and ^{15}N) MAS NMR spectra are provided in Figures S22 and S33.

Thermal Characterization. Thermal gravimetric analysis (TGA) was carried out on a PerkinElmer TGA8000 instrument. About 3−5 mg of sample was placed in a ceramic crucible, and the experiment was performed from 30 to 600 °C at a heating rate of 10 °C min^{-1}. A PerkinElmer DSC6000 instrument was used for differential scanning calorimetry (DSC). For each experiment, ca. 2−4 mg of sample was sealed in an aluminum pan, and the experiment was performed under the N_2 gas atmosphere to exclude contact with the moisture or the air. Specifically, DSC experiments were carried out from −80 to 200 °C at a heating rate of 5 °C min^{-1}. The intersection of the baseline and the tangent was determined using Pyris software to obtain the onset of the decomposition temperature (T_{decomp}) and the glass transition temperature (T_g). The melting points (T_m) were obtained similarly from the DSC traces and also using an Electrothermal IA9000 Series Melting Point Apparatus, respectively.

The area under the DSC trace gives the enthalpy (ΔH) for a transition and is related to the change in entropy (ΔS) and the change in Gibbs free energy (ΔG) of a reaction according to the following (eq 1)

$$\Delta G = \Delta H - T\Delta S \quad (1)$$

Where T is the absolute temperature in Kelvin (K). When solid−solid transitions and solid−liquid (melting) phase transitions are reversible, ΔG in the equilibrium process equals to zero, and thus, ΔS of all these phase transitions can be expressed as the following eq (eq 2), which was used to analyze the molar entropies for the ionic materials

$$\Delta S = \frac{\Delta H \times M}{T} \quad (2)$$

Where M is the molecular weight (in g mol^{-1}) of the bulk material.

FTIR Spectroscopy. A Bruker Tensor 27 FTIR spectrometer was used for FTIR spectroscopy. KBr pellets were made using a manual hydraulic press from Specac, UK. The FTIR spectra were recorded in the range from 400 to 4000 cm^{-1} with 64 scans and with a resolution of 4 cm^{-1}.

Ionic Conductivity. A Metrohm Autolab PGSTAT302N electrochemical workstation with an FRA32 M module was used for measurements of the ionic conductivity, and the data were processed using the Nova 2.1 software. A TSC 70 closed cell coupled to a temperature-controller Microcell HC (rhd Instruments, Germany) with ±0.1 °C accuracy was used for all liquid samples. The ionic conductivities were determined using electrochemical impedance spectroscopy (EIS) in the frequency range from 1 Hz to 1 MHz with an AC voltage amplitude of 10 mV_{rms} and a temperature range from −30 to 100 °C. A two-electrode setup was used for the assessment with a glassy carbon electrode (GC, diameter = 2 mm) and a 70 μL Pt crucible as the counter electrode (K_{cell} = 1.8736 cm^{-1}). The cell was thermally equilibrated for 10 min before each experiment.

A TSC battery cell, coupled to a temperature-controller Microcell HC (rhd Instruments, Germany), with stainless steel disks as current collectors freshly polished by Kemet diamond paste (average particle size of ∼250 nm) was employed for solid samples. In the case of solid samples with T_m < 100 °C, a 0.2 mm spacer sandwiched between the two disc electrodes was used to control thickness of the film (K_{cell} = 0.039789 cm^{-1}). The powder sample was packed inside the cell and kept at 100 °C for 30 min to melt the sample, followed by cooling of the sample to ambient temperature, and the measurement was started after keeping the sample at ambient temperature for 1 h. For samples with T_m > 100 °C, pellets with known thickness were made using a manual hydraulic press and the pellets were dried in a vacuum oven at 80 °C for 3 days prior to each experiment. The cell was thermally equilibrated for 20 min before each experiment.

Single-Crystal X-ray Diffraction. Single-crystal X-ray diffraction (SC-XRD) studies were carried out on [P_{4444}][BGB] and [N_{4444}][BGB] using crystals coated with NVH oil, mounted at the end of a cryoloop, and placed in the nitrogen cold stream (100 and 293 K) of an Xcalibur Eos diffractometer. The deviations of experimental temperatures are ±2 K. Data were collected using MoKα radiation, and empirical absorption correction was carried out using spherical harmonics, implemented in the SCALE3 ABSPACK scaling algorithm (CrysAlisPro 1.171.42.89a; Rigaku Oxford Diffraction, 2023). The crystal structures were solved using SHELXT (intrinsic phasing) and refined using SHELXL-2018 (least-squares),[33,34] with data processing carried out in Olex2.[35]

https://doi.org/10.1021/acs.cgd.4c01030
Cryst. Growth Des. 2024, 24, 8989−8998

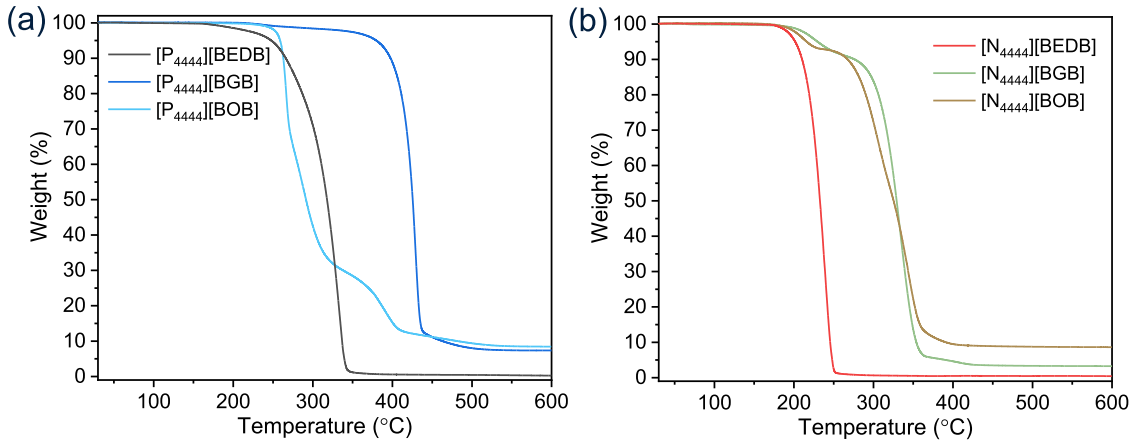

Figure 2. TGA curves of (a) phosphonium-based and (b) ammonium-based orthoborate ionic materials.

RESULTS AND DISCUSSION

Here, we present a brief description of the thermal stability and phase behavior, followed by an assessment of the ionic conductivities of the orthoborate ionic materials. Next, the solid-state cation−anion interactions are systematically described with the help of FTIR and multinuclear (^{15}N, ^{31}P, ^{13}C, and ^{11}B) solid-state NMR spectroscopy data, and finally, the crystal structures of two ionic materials at different temperatures are presented.

Thermal Properties. Thermal stabilities of the salts are significantly affected by the type of cation and the presence of carbonyl groups in the orthoborate anion (Figure 2). For a common anion, the salts with phosphonium cations exhibit higher thermal stabilities than those with ammonium cations, which agrees well with previous findings.[36] Overall, the T_{decomp} of the salts follows the sequence: [P_{4444}][BGB] > [P_{4444}][BOB] > [P_{4444}][BEDB] and [N_{4444}][BGB] > [N_{4444}][BOB] > [N_{4444}][BEDB]. Thus, the salts with [BGB] anions are the most thermally stable, while the salts with [BEDB] anions are the least stable (Table S1). In addition, both [N_{4444}][BOB] and [N_{4444}][BGB] revealed two-step decomposition paths; the first step with approximately 10% weight loss and the second with more than 80% weight loss. Among the six salts, [P_{4444}][BGB] displayed the highest T_{decomp} value of about 400 °C.

The DSC traces reveal solid−solid phase transitions before melting (Figure 3). The DSC traces of [P_{4444}][BEDB] and [P_{4444}][BGB] indicate repeatable phase transitions in two consecutive cycles, while the salts with the [N_{4444}] cation display slightly different thermal behavior in the second consecutive heating cycle. The peak #1 in these four solid ionic materials is the melting process, which is further confirmed by a melting point apparatus (Table S2). These ionic materials remain in plastic phases over different temperature ranges. Since the entropies of fusion (ΔS_{fus}) for these four salts are >20 J mol^{-1} K^{-1} (Table S3) and they thus do not obey Timmermans' criterion,[37] not all of these ionic materials can be classified as plastic crystals.[38,39] As the Timmermans' criterion was originally developed for simple molecular crystalline materials, but in our case, each material comprises cations and anions, making the system much more complex, e.g., only one ion might be involved in the rotational motions in the solid state, while the other exhibits rotational degrees of freedom only upon melting and, therefore, lead to a higher residual entropy of fusion. This has been observed for a series of ionic materials based on pyrrolidinium cations coupled to the bis-(trifluoromethanesulfonyl) i/amide (TFSI/A) anion, exhibiting ΔS_{fus} of 40−80 J mol^{-1} K^{-1}.[38] Similarly, the dimethylammonium perrhenate plastic crystal displayed a ΔS_{fus} of 38.2 J mol^{-1} K^{-1} attributed to the formation of a rotator phase before melting.[39]

Both [P_{4444}][BEDB] and [N_{4444}][BEDB] exhibit relatively higher T_m, 158 and 169 °C, respectively (Table S2). [P_{4444}][BEDB] displays a solid−solid phase transition at −59 °C, ΔS_{II-I} of which is larger than that of [N_{4444}][BEDB] (25 vs 10 J mol^{-1} K^{-1}), and remains in plastic phase I over a very wide temperature range from −59 to 158 °C (Table S3), which is much broader than for other reported OIPC materials.[23,25] On the other hand, [N_{4444}][BEDB] stays in phase I from 80 to 169 °C. The salts with the [BGB] anion have much lower T_m: 64 and 80 °C for [P_{4444}][BGB] and [N_{4444}][BGB], respectively (Table S2), and among the four ionic materials, [P_{4444}][BGB] has the largest ΔS_{II-I}: 51 J mol^{-1} K^{-1} and [N_{4444}][BGB] has ΔS_{II-I} of ca. 1 J mol^{-1} K^{-1}. Unlike [N_{4444}][BGB], remaining in phase I over a temperature range from 69 to 80 °C, [P_{4444}][BGB] exhibits phase I over a larger temperature range from −6 to 64 °C, which can be particularly beneficial for applications as a solid-state electrolyte. Unlike the other salts, the second cycle of [N_{4444}][BGB] differs from the first one in terms of phase transitions and entropies (Table S4); there is an extra phase III evolved followed by a very narrow phase II in the range from 55 to 59 °C. Notably, ΔS_{fus} from the second cycle is much smaller compared to the first one: 23 vs 110 J mol^{-1} K^{-1}.

The RTIL [N_{4444}][BOB] exhibits glass transition temperature, T_g = −33 °C, while [P_{4444}][BOB] exhibits a typical supercooled liquid behavior;[40] the glass transition/liquid−liquid transition at −58 °C is followed by a cold crystallization and subsequent melting (Figure 3e,f). A similar thermal phase behavior is observed for trihexyl(tetradecyl)phosphonium thiocyanate [$P_{666,14}$][SCN] as well as trihexyl(tetradecyl)-phosphonium borohydride [$P_{666,14}$][BH_4] ILs.[40] The DSC data clearly show that the T_m decreases with an increase in the number of carbonyl groups of the anion, pointing to the importance of cation−anion interactions for the thermal stability, also important for the ion mobility and ionic conductivity.

Ionic Conductivities. A comparison of the ionic conductivities of the RTILs and ionic materials is presented in Figure 4. For the RTILs, the ionic conductivity of [P_{4444}][BOB] is higher than that of [N_{4444}][BOB] over the whole studied temperature range, especially at lower temperatures. This agrees

https://doi.org/10.1021/acs.cgd.4c01030
Cryst. Growth Des. 2024, 24, 8989−8998

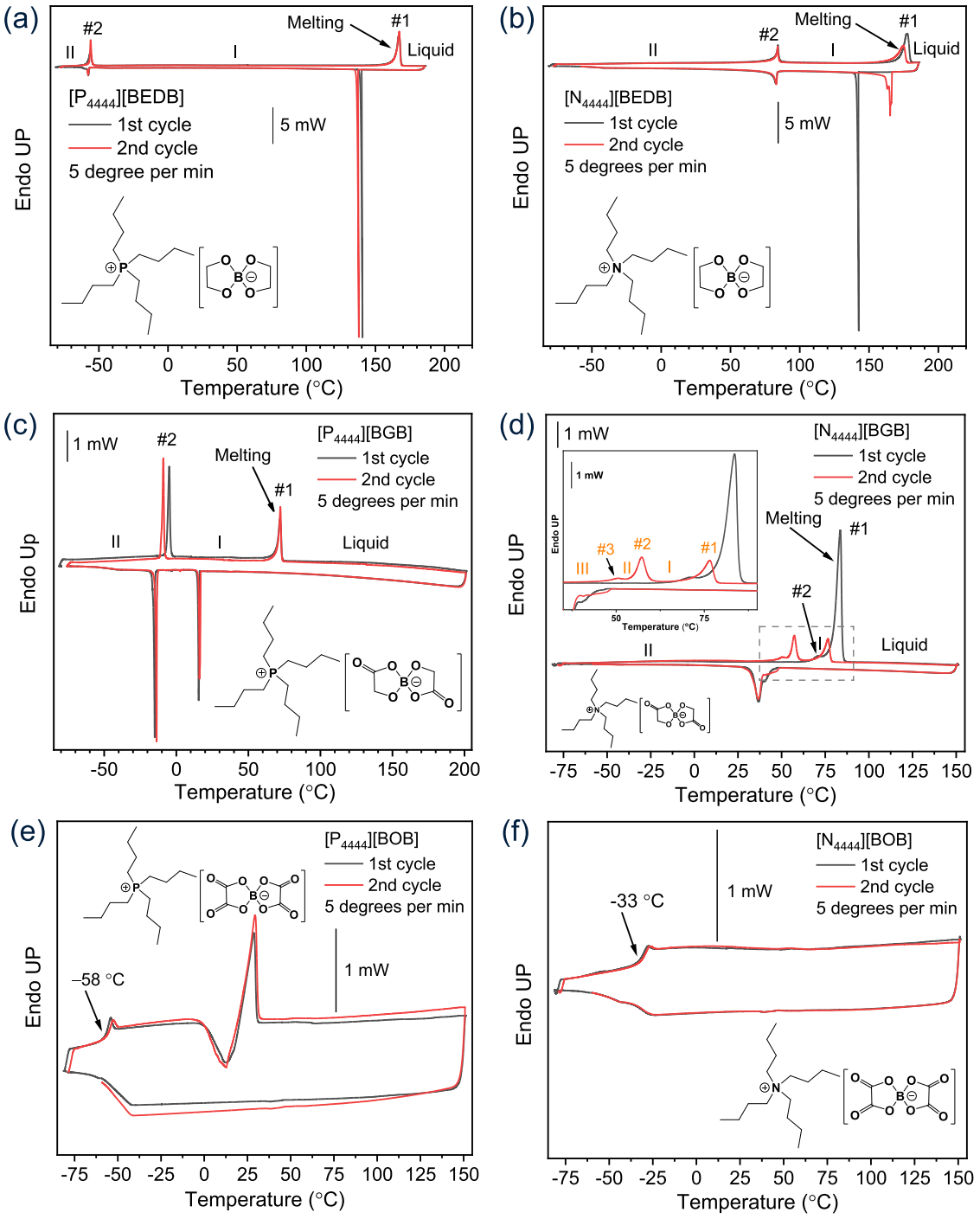

Figure 3. DSC traces of (a) $[P_{4444}][BEDB]$, (b) $[N_{4444}][BEDB]$, (c) $[P_{4444}][BGB]$, (d) $[N_{4444}][BGB]$, (e) $[P_{4444}][BOB]$, and (f) $[N_{4444}][BOB]$.

well with the previously published data for RTILs with the 2-[2-(2-methoxyethoxy)ethoxy]acetate [MEEA] anion, $[P_{4444}]$-[MEEA] and $[N_{4444}]$[MEEA], where the phosphonium RTIL exhibited a ~ 1.6-fold higher ionic conductivity (~0.1 vs ~ 0.06 mS cm^{-1} at 20 °C).[36] The same is true for the ionic materials, as $[P_{4444}][BGB]$ has over one order-of-magnitude higher ionic conductivities than the molecularly analogous $[N_{4444}][BGB]$ salt (2.3×10^{-3} vs 1.0×10^{-4} mS cm^{-1} at 20 °C).

Since $[P_{4444}][BGB]$ melts at 64 °C, the ionic conductivities of all of the orthoborate salts in this study are tabulated at 20 and 60 °C for a fair comparison between different ionic materials (Table S5). The ionic conductivities of $[P_{4444}][BGB]$ and $[N_{4444}]$-[BEDB] are comparable at both 20 and 60 °C. Among the solid ionic materials, $[N_{4444}][BGB]$ showed the lowest ionic conductivities throughout the whole studied temperature range, which is attributed to its lowest degree of disorder and strongest ionic interactions among systems in this study (see below). Consider that the method used for solid samples (with melting points of <100 °C), the change of ionic conductivity for $[N_{4444}][BGB]$ likely fits better to its DSC trace from the second cooling−heating cycle. On the other hand, the RTIL $[P_{4444}][BOB]$ displays the highest ionic conductivities, which might be due to its weak ionic interactions.

https://doi.org/10.1021/acs.cgd.4c01030
Cryst. Growth Des. 2024, 24, 8989−8998

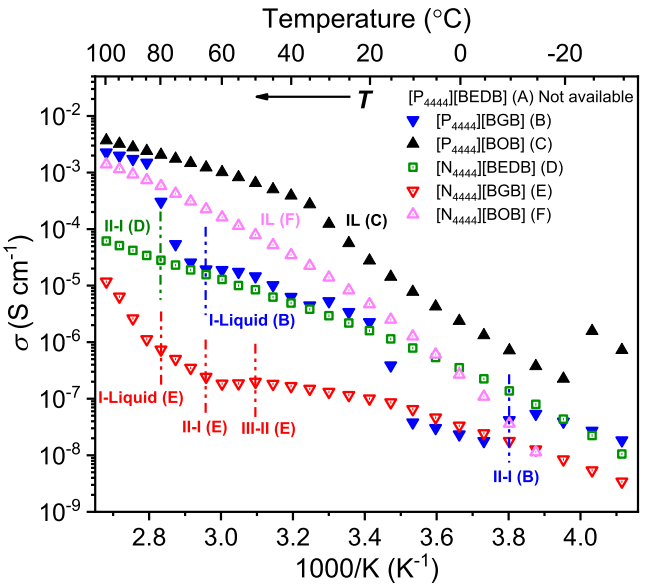

Figure 4. Ionic conductivities of organic orthoborate ionic materials. The data are taken from the first heating cycles.

Ionic Interactions, Structure, and Morphology. Ionic interactions were investigated using both FTIR and solid-state NMR spectroscopy, while structures were assessed by SC-XRD. FTIR spectroscopy is primarily employed to explore the cation−anion interactions in these ionic materials, due to its excellent sensitivity toward coordination changes to the functional groups of the orthoborate anions. The FTIR spectra reflect the structural differences between the salts as, e.g., the C═O stretching mode (1850−1650 cm^{-1}) of $[P_{4444}][BOB]$ and $[N_{4444}][BOB]$, which displays broad bands with multiple peaks around 1813 and 1780 cm^{-1} with shoulders on both sides, while $[P_{4444}][BGB]$ and $[N_{4444}][BGB]$ show relatively sharp single peaks at 1737 cm^{-1} (Figure 5). The [BGB] anion contains only one C═O group on each side of the boron atom, and the relative red shift implies stronger interactions within borate anions.[41,42]

The solid-state multinuclear (^{15}N, ^{31}P, ^{13}C, and ^{11}B) NMR spectroscopy provides additional information about the structure, dynamics, and cation−anion interactions in the ionic materials. The ^{15}N CP-MAS NMR revealed that the nitrogen atom in the cation of $[N_{4444}][BGB]$, in which the anion [BGB] has two carbonyl groups, is additionally deshielded by *ca.* 3 ppm as compared to the nitrogen atom in $[N_{4444}][BEDB]$, in which the anion [BEDB] has no carbonyl groups in its structure (Figure 6a). This further supports that the polar carbonyl groups, which are electron-withdrawing by inductive effects, play a key role in the ionic interactions[43] and is further confirmed by the ^{31}P CP-MAS NMR spectra of the phosphonium-based salts (Figure 6b). Again, the ^{31}P NMR resonance line of $[P_{4444}][BGB]$ is observed at a higher chemical shift compared to its structural analogue without any carbonyl groups, i.e., $[P_{4444}][BEDB]$. However, the additional deshielding of the P atoms in the former salt is considerably smaller (*ca.* 0.5 ppm for ^{31}P vs *ca.* 3 ppm for ^{15}N), that despite higher sensitivity of isotropic chemical shifts of ^{15}N to the structural changes, they still point to weaker cation−anion interactions in $[P_{4444}][BGB]$ as compared to $[N_{4444}][BGB]$.

The ^{13}C CP-MAS NMR spectra revealed resonance lines in the range from 172 to 180 ppm and 60 to 72 ppm, which are assigned to carbon sites in C═O and [−C(O)−] groups of anions [BEDB] and [BGB] in ionic materials, respectively (Figure 6c). The phosphonium-based salts display single resonance lines for C═O and [−C(O)−] groups, while pairs of resonance lines for these carbon sites are observed for the ammonium-based salts. This clearly indicates that the carbon atoms are chemically inequivalent in the latter, either in the same anion or in two anions having different conformations in the asymmetric unit, as in bis(salicylato)borate salts reported previously.[44] Additional broadening and characteristic "molecular-motion-distorted" line shapes of resonance lines in the spectrum of $[P_{4444}][BGB]$ could be due to conformational and rotational dynamics of anions in this ionic material at the ambient temperature of the ^{13}C CP-MAS NMR experiment (293 K), which is correlated with the ionic conductivity data (an abrupt change in conductivity from ca 10^{-8} to 10^{-6} S cm^{-1}) nearby this temperature (see blue triangles in Figure 4).

^{11}B single-pulse MAS NMR spectra of these ionic materials display a single resonance line for the boron atom in anions for all salts in this study (Figure 6d). Although the chemical shifts are very similar, the ^{11}B resonance lines of the ammonium-based salts are significantly broader (Table S6), suggesting either larger structural distortions in the BO_4 moiety (^{11}B is a quadrupolar nucleus with spin $I = 3/2$) or the presence of orthoborate anions with different conformations in these ammonium salts.[45]

In view of the fact that $[P_{4444}][BGB]$ and $[N_{4444}][BGB]$ crystallize well, we characterized these salts in the solid state by SC-XRD to get deeper insights into their structure (Figure 7). The $[N_{4444}][BGB]$ crystallizes in the triclinic space-group $P\bar{1}$, whereas the $[P_{4444}][BGB]$ crystallizes in the monoclinic space-group $C2/c$. In each case, a borate ion forms a spirocyclic motif, with the central boron atom coordinated by two chelating glycolate ions, each bound through an alcoholate group and a carboxylate group. Notable structural features within the borate ions are that the $B-O_{alcoholate}$ bonds are shorter (O6−B1, O3−B1 = 1.414(5)−1.449(2) Å) than the $B-O_{carboxylate}$ bonds (O4−B1, O1−B1 = 1.497(6)−1.515(5) Å) (Figures S34−S35 and Tables S7−S11). Moreover, in the five-membered chelate rings, the glycolate carboxylate carbons distort away from an idealized trigonal planar geometry (all bond angles at 120°), resulting in smaller $C-C-O_{carboxylate-B}$ angles (C4−C3−O4, C2−C1−O1 = 108.9(1)−109.0(1)°). These angles approach the bond angle

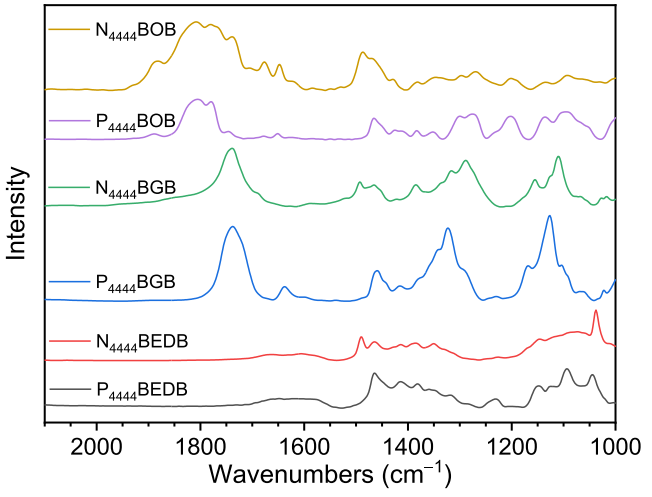

Figure 5. FTIR spectra of the orthoborate salts in the range from 2100 to 1000 cm^{-1}.

https://doi.org/10.1021/acs.cgd.4c01030
Cryst. Growth Des. 2024, 24, 8989−8998

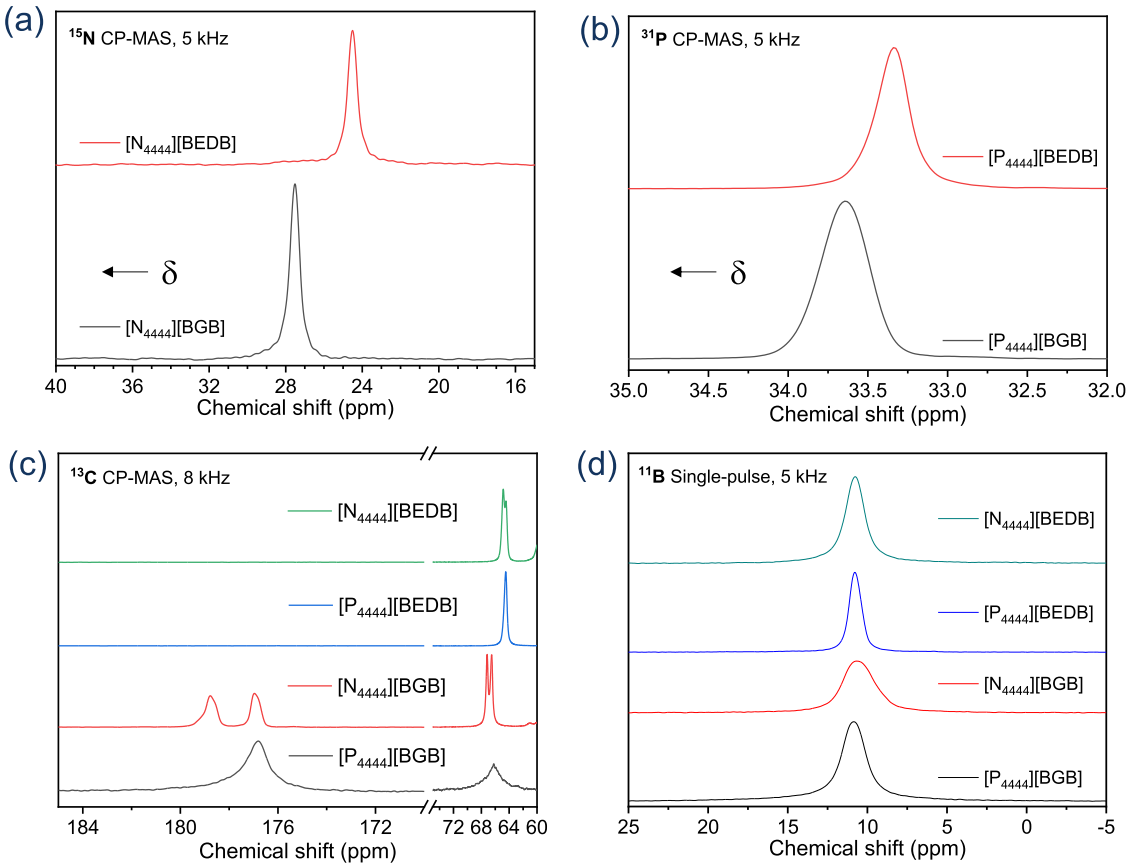

Figure 6. Solid-state NMR spectra of the ionic materials: (a) ^{15}N CP-MAS, (b) ^{31}P CP-MAS, (c) ^{13}C CP-MAS (parts of the spectra corresponding to anions), and (d) ^{11}B single-pulse MAS NMR spectra. The MAS frequencies were 5 kHz in Figure 6a, 6b, and 6d and 8 kHz in Figure 6c. The numbers of signal transients were 77 238 and 84 084 from top to bottom in Figure 6a, 4 in Figure 6b, 1358, 1358, 3978, and 3978 from top to bottom in Figure 6c, and (d) 64 in Figure 6d.

expected for a regular pentagon (108°), showing how the glycolate ion distorts when it becomes part of a chelate ring with boron.

Furthermore, when inspecting the C−C−C−C torsion angles of the butyl groups, it can be seen that all butyls in [N_{4444}][BGB] assume a zigzag conformation (176.8(1)−179.2(1)°). Similarly, three of the butyl groups in [P_{4444}][BGB] assume a zigzag conformation (171.4(4)−179.4(4)°), whereas the fourth assumes a coiled conformation (torsion angle 69.9(5)°). The [BGB] ions have one C═O group showing three contacts and another C═O group showing one contact to the cations. This is both the case for the [P_{4444}] and for the [N_{4444}] salt. It is, however, notable that the contacts involve two [P_{4444}] cations in [P_{4444}][BGB] but three [N_{4444}] cations in [N_{4444}][BGB] (Figure S35 and Table S12). These structural features could be correlated with the solid-state NMR data, where the [N_{4444}] cation affects the [BGB] anion by giving rise to two ^{13}C resonance lines for the carbon atoms and the broadness of the ^{11}B resonance line. Thus, despite their chemically similar composition, [N_{4444}][BGB] and [P_{4444}][BGB] pack in entirely different ways, in line with their disparate physical properties.

For [N_{4444}][BGB], the crystal packing is defined by space group $P\bar{1}$ at both 100 and 293 K (corresponding to Phase II), and the packing is essentially isostructural at these temperatures (Figure S36). At the higher temperature, the thermal ellipsoids become larger, and the cell distances, a and b, increase significantly, from 9.5669(3) to 9.7009(6) Å and 10.9146(3) to 11.0731(6) Å. On the other hand, c only increases from 12.4087(4) to 12.4567(7) Å. At the same time, the cell angle, γ, increases from 64.783(3)° to 65.628(5)°, whereas α and β are almost unchanged.

In contrast, for [P_{4444}][BGB], the crystal packing changes from space group $C2/c$ at 100 K (Phase II) to $P\bar{1}$ at 293 K (Phase I, two crystallographically independent formula units per unit cell in the triclinic case). The close similarity in crystal packing for [P_{4444}][BGB] can be seen by viewing the triclinic and monoclinic crystal structures along the crystallographic c-axes, which gives a reasonably good overlay (Figure 8). The room-temperature structure shows large thermal ellipsoids, and the disorder in several of the butyl chains of the cations is noticeable. It is also noticeable that whereas the unit cell volume increases only slightly when [N_{4444}][BGB] goes from 100 to 293 K (1117.99(7) Å^3 to 1162.55(13) Å^3), the unit cell volume for [P_{4444}][BGB] goes from 4660.7(5) Å^3 (monoclinic) to 2530.86(16) Å^3 (triclinic) when the temperature increases, i.e., a volume expansion of 8.6% per formula unit of [P_{4444}][BGB]. Although no visible phase transitions are detected in the DSC curves upon heating from 10 to 50 °C, there exists an obvious increase in the ionic conductivity of [P_{4444}][BGB] from 10 to 20 °C, which agrees well with the structural changes.

CONCLUSIONS

The presence of electron-withdrawing carbonyl groups in the orthoborate anions plays a key role in their ionic interactions as well as structures and fundamental properties. The salts totally

https://doi.org/10.1021/acs.cgd.4c01030
Cryst. Growth Des. 2024, 24, 8989−8998

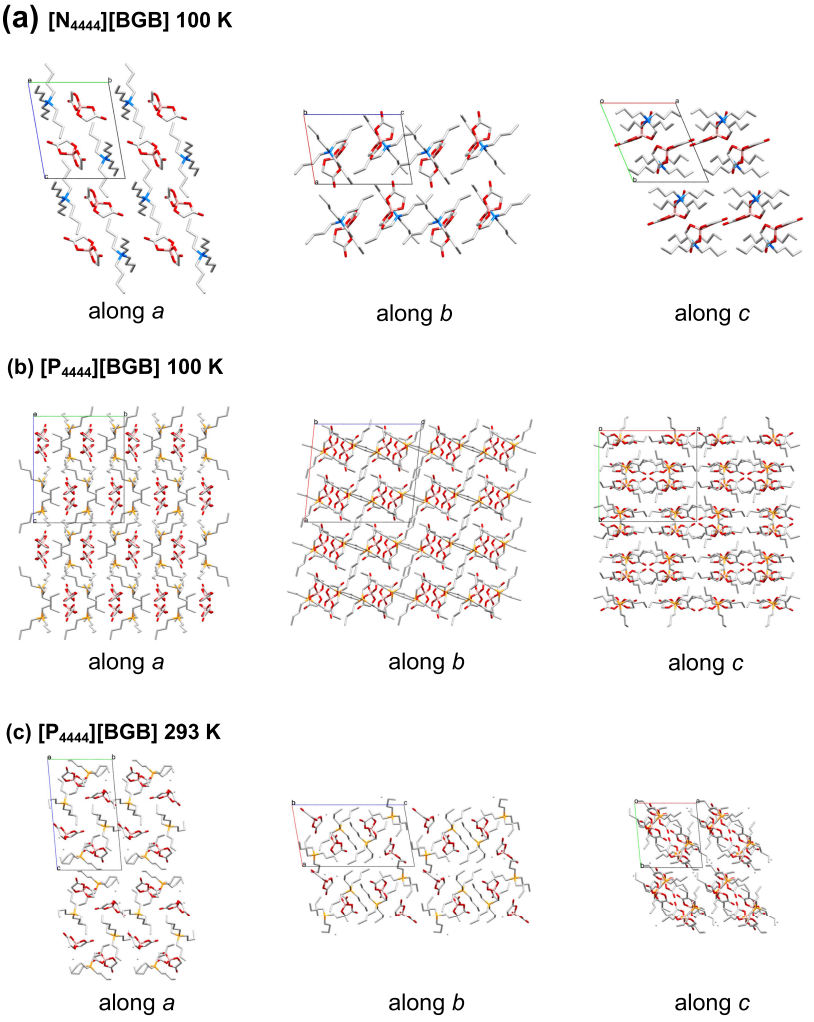

Figure 7. Crystal packing showing 2 × 2 × 2 unit cells viewed along the crystallographic *a*-axis, *b*-axis, and *c*-axis. (a) $[N_{4444}][BGB]$ at 100 K, and (b, c) $[P_{4444}][BGB]$ at 100 and 293 K, respectively.

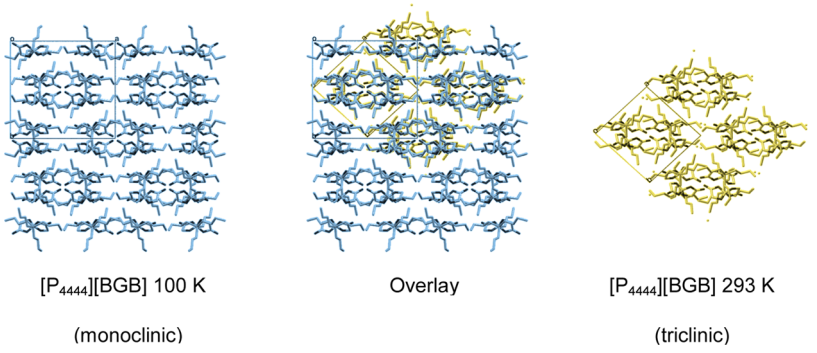

Figure 8. Change of the crystal packing for $[P_{4444}][BGB]$ from monoclinic at 100 K to triclinic at 293 K.

without and with two carbonyl groups in their anions, i.e., the [BEDB] and [BGB], exhibit plastic crystal behavior, while the [BOB]-based salts containing four carbonyl groups remain liquid at ambient temperature. The [BGB] anion-based salts revealed superior thermal stability, and their structures are significantly affected by the countercation, as confirmed by FTIR, X-ray crystallographic studies, and multinuclear solid-state NMR spectroscopy. This work sheds light on the structure−property relationship of orthoborate-based ionic materials and will facilitate the structural designability of fluorine-free organic ionic plastic crystals for energy storage applications.

■ ASSOCIATED CONTENT

Supporting Information

The Supporting Information is available free of charge at https://pubs.acs.org/doi/10.1021/acs.cgd.4c01030.

Solution sate (^{1}H, ^{13}C, ^{11}B, and ^{31}P) NMR spectra; solid-state (^{13}C, ^{11}B, ^{31}P, and ^{15}N) MAS NMR spectra; decomposition and phase transition temperatures;

https://doi.org/10.1021/acs.cgd.4c01030
Cryst. Growth Des. 2024, 24, 8989−8998

comparison of ionic conductivity; line widths of resonance lines for solid-state ^{11}B MAS NMR spectra; X-ray crystallographic studies (PDF)

Accession Codes

CCDC 2337095−2337096 contain the supplementary crystallographic data for this paper. These data can be obtained free of charge via www.ccdc.cam.ac.uk/data_request/cif, or by emailing data_request@ccdc.cam.ac.uk, or by contacting The Cambridge Crystallographic Data Center, 12 Union Road, Cambridge CB2 1EZ, UK; fax: +44 1223 336033.

AUTHOR INFORMATION

Corresponding Authors

Patrik Johansson − *Department of Physics, Chalmers University of Technology, SE-412 96 Gothenburg, Sweden; ALISTORE-European Research Institute, 80039 Amiens, France;* orcid.org/0000-0002-9907-117X; Email: patrik.johansson@chalmers.se

Faiz Ullah Shah − *Chemistry of Interfaces, Luleå University of Technology, SE-971 87 Luleå, Sweden;* orcid.org/0000-0003-3652-7798; Email: faiz.ullah@ltu.se

Authors

Yanqi Xu − *Chemistry of Interfaces, Luleå University of Technology, SE-971 87 Luleå, Sweden;* orcid.org/0000-0003-3803-2705

Anders Reinholdt − *Centre for Analysis and Synthesis, Lund University, SE-221 00 Lund, Sweden;* orcid.org/0000-0001-6637-8338

Oleg N. Antzutkin − *Chemistry of Interfaces, Luleå University of Technology, SE-971 87 Luleå, Sweden*

Maria Forsyth − *Institute for Frontier Materials (IFM), Deakin University, Burwood 3125 Victoria, Australia;* orcid.org/0000-0002-4273-8105

Complete contact information is available at: https://pubs.acs.org/10.1021/acs.cgd.4c01030

Notes

The authors declare no competing financial interest.

ACKNOWLEDGMENTS

The authors gratefully acknowledge financial support from the Swedish Research Council for Sustainable Development (Grant number: 2020-00969), and P.J. is also grateful for the financial support from his Swedish Research Council (VR) Distinguished Professor grant "Next Generation Batteries" (#2021-00613). The Foundation in memory of J.C. and Seth M. Kempe (project numbers JCK-1306 and JCK-1433) and the laboratory found at LTU are acknowledged for providing grants, from which a Bruker Aeon/Avance III NMR spectrometer at LTU has been purchased.

REFERENCES

(1) Shah, F. U.; Glavatskih, S.; Antzutkin, O. N. Boron in Tribology: From Borates to Ionic Liquids. *Tribol. Lett.* **2013**, *51*, 281−301.

(2) Das, B. C.; Thapa, P.; Karki, R.; Schinke, C.; Das, S.; Kambhampati, S.; Banerjee, S. K.; Van Veldhuizen, P.; Verma, A.; Weiss, L. M.; Evans, T. Boron Chemicals in Diagnosis and Therapeutics. *Fut. Med. Chem.* **2013**, *5*, 653−676.

(3) Chauhan, N. P. S.; Hosmane, N. S.; Mozafari, M. Boron-Based Polymers: Opportunities and Challenges. *Mater. Today Chem.* **2019**, *14*, No. 100184.

(4) Huang, Z.; Wang, S.; Dewhurst, R. D.; Ignat'ev, N. V.; Finze, M.; Braunschweig, H. Boron: Its Role in Energy-Related Processes and Applications. *Angew. Chem., Int. Ed.* **2020**, *59*, 8800−8816.

(5) Adams, J.; Behnke, M.; Chen, S.; Cruickshank, A. A.; Dick, L. R.; Grenier, L.; Klunder, J. M.; Ma, Y.-T.; Plamondon, L.; Stein, R. L. Potent and Selective Inhibitors of the Proteasome: Dipeptidyl Boronic Acids. *Bioorg. Med. Chem. Lett.* **1998**, *8*, 333−338.

(6) Xu, W.; Angell, C. A. LiBOB and Its Derivatives: Weakly Coordinating Anions, and the Exceptional Conductivity of Their Nonaqueous Solutions [Electrochem. Solid-State Lett., 4, E1 (2001)]. *Electrochem. Solid-State Lett.* **2001**, *4*, L3.

(7) Xu, K.; Zhang, S.; Jow, T. R.; Xu, W.; Angell, C. A. LiBOB as Salt for Lithium-Ion Batteries: A Possible Solution for High Temperature Operation. *Electrochem. Solid-State Lett.* **2002**, *5*, A26.

(8) Mogensen, R.; Colbin, S.; Menon, A. S.; Björklund, E.; Younesi, R. Sodium Bis(oxalato)borate in Trimethyl Phosphate: A Fire-Extinguishing, Fluorine-Free, and Low-Cost Electrolyte for Full-Cell Sodium-Ion Batteries. *ACS Appl. Energy Mater.* **2020**, *3*, 4974−4982.

(9) Guzmán-Torres, J.; Ochoa-Gamboa, D. L.; Garza-Tovar, L. L.; Torres-González, L. C.; de la Parra-Arciniega, S. M.; González-Juárez, E.; Gómez, I.; Sánchez, E. M. Magnesium Bis(Oxalate)Borate as a Potential Electrolyte for Rechargeable Magnesium Ion Batteries. *J. Electron. Mater.* **2023**, *52*, 1250−1257.

(10) Hayamizu, K.; Matsuo, A.; Arai, J. A Divalent Lithium Salt $Li_2B_{12}F_{12}$ Dissolved in Propylene Carbonate Studied by NMR Methods. *J. Electrochem. Soc.* **2009**, *156*, A744.

(11) Fisher, S. P.; Tomich, A. W.; Lovera, S. O.; Kleinsasser, J. F.; Guo, J.; Asay, M. J.; Nelson, H. M.; Lavallo, V. Nonclassical Applications of closo-Carborane Anions: From Main Group Chemistry and Catalysis to Energy Storage. *Chem. Rev.* **2019**, *119*, 8262−8290.

(12) Haskins, J. B.; Bennett, W. R.; Wu, J. J.; Hernández, D. M.; Borodin, O.; Monk, J. D.; Bauschlicher, C. W., Jr.; Lawson, J. W. Computational and Experimental Investigation of Li-Doped Ionic Liquid Electrolytes: [pyr14][TFSI], [pyr13][FSI], and [EMIM][BF_4]. *J. Phys. Chem. B* **2014**, *118*, 11295−11309.

(13) Basile, A.; Hilder, M.; Makhlooghiazad, F.; Pozo-Gonzalo, C.; MacFarlane, D. R.; Howlett, P. C.; Forsyth, M. Ionic Liquids and Organic Ionic Plastic Crystals: Advanced Electrolytes for Safer High Performance Sodium Energy Storage Technologies. *Adv. Energy Mater.* **2018**, *8*, No. 1703491.

(14) Thomas, M. L.; Hatakeyama-Sato, K.; Nanbu, S.; Yoshizawa-Fujita, M. Organic Ionic Plastic Crystals: Flexible Solid Electrolytes for Lithium Secondary Batteries. *Energy Adv.* **2023**, *2*, 748−764.

(15) Jin, L.; Howlett, P. C.; Pringle, J. M.; Janikowski, J.; Armand, M.; MacFarlane, D. R.; Forsyth, M. An Organic Ionic Plastic Crystal Electrolyte for Rate Capability and Stability of Ambient Temperature Lithium Batteries. *Energy Environ. Sci.* **2014**, *7*, 3352−3361.

(16) Zhou, Y.; Wang, X.; Zhu, H.; Armand, M.; Forsyth, M.; Greene, G. W.; Pringle, J. M.; Howlett, P. C. Ternary Lithium-Salt Organic Ionic Plastic Crystal Polymer Composite Electrolytes for High Voltage, All-Solid-State Batteries. *Energy Storage Mater.* **2018**, *15*, 407−414.

(17) Liao, Z.; Hu, A.; Huang, C.; Zhao, E.; Orit, A.; Zhang, Z.; Yang, L. Long-Cycling High-Voltage Lithium Metal Batteries Enabled by Anion-Concentrated Plastic Crystal Electrolytes. *Chem. Eng. J.* **2023**, *461*, No. 141382.

(18) Kim, B.; Yang, S. H.; Seo, J.-H.; Kang, Y. C. Inducing an Amorphous Phase in Polymer Plastic Crystal Electrolyte for Effective Ion Transportation in Lithium Metal Batteries. *Adv. Funct. Mater.* **2024**, *34*, No. 2310957.

(19) Makhlooghiazad, F.; Gunzelmann, D.; Hilder, M.; MacFarlane, D. R.; Armand, M.; Howlett, P. C.; Forsyth, M. Mixed Phase Solid-State Plastic Crystal Electrolytes Based on a Phosphonium Cation for Sodium Devices. *Adv. Energy Mater.* **2017**, *7*, No. 1601272.

(20) Plylahan, N.; Kerner, M.; Lim, D.-H.; Matic, A.; Johansson, P. Ionic Liquid and Hybrid Ionic Liquid/Organic Electrolytes for High Temperature Lithium-Ion Battery Application. *Electrochim. Acta* **2016**, *216*, 24−34.

(21) Bhowmick, S.; Filippov, A.; Khan, I. A.; Shah, F. U. Physical and Electrochemical Properties of New Structurally Flexible Imidazolium

Phosphate Ionic Liquids. *Phys. Chem. Chem. Phys.* **2022**, *24*, 23289−23300.
(22) Yamada, H.; Miyachi, Y.; Takeoka, Y.; Rikukawa, M.; Yoshizawa-Fujita, M. Pyrrolidinium-based Organic Ionic Plastic Crystals: Relationship between Side Chain Length and Properties. *Electrochim. Acta* **2019**, *303*, 293−298.
(23) Abu-Lebdeh, Y.; Alarco, P.-J.; Armand, M. Conductive Organic Plastic Crystals Based on Pyrazolium Imides. *Angew. Chem., Int. Ed.* **2003**, *42*, 4499−4501.
(24) Lan, X.; Wang, X.; Zhang, D. X.; Mu, T.; Lan, X. Z. Cation and Anion Transfer in Quinuclidinium Hexafluorophosphate Plastic Crystal: Role of Constituent Ions and the Crystalline Structure. *J. Phys. Chem. C* **2021**, *125*, 21169−21178.
(25) Iranipour, N.; Gunzelmann, D. J.; Seeber, A. J.; Vongsvivut, J.; Hollenkamp, A. F.; Forsyth, M.; Howlett, P. C. Effect of Secondary Phase on Thermal Behaviour and Solid-State Ion Conduction in Lithium Doped N-ethyl-N-methylpyrrolidinium Tetrafluoroborate Organic Ionic Plastic Crystal. *J. Mater. Chem. A* **2017**, *5*, 24909−24919.
(26) Kang, C. S. M.; Hutt, O. E.; Pringle, J. M. Halide-Free Synthesis of New Difluoro(oxalato)borate [DFOB]−Based Ionic Liquids and Organic Ionic Plastic Crystals. *ChemPhysChem* **2022**, *23*, No. e202200115.
(27) Yunis, R.; Newbegin, T. W.; Hollenkamp, A. F.; Pringle, J. M. Ionic Liquids and Plastic Crystals with a Symmetrical Pyrrolidinium Cation. *Mater. Chem. Front.* **2018**, *2*, 1207−1214.
(28) Abeysooriya, S.; Makhlooghiazad, F.; Chotard, J.-N.; O'Dell, L. A.; Pringle, J. M. Investigation of the Physicochemical Properties of Pyrrolidinium-Based Mixed Plastic Crystal Electrolytes. *J. Phys. Chem. C* **2023**, *127*, 12304−12320.
(29) Ue, M.; Shima, K.; Mori, S. Electrochemical Properties of Quaternary Ammonium Borodiglycolates and Borodioxalates. *Electrochim. Acta* **1994**, *39*, 2751−2756.
(30) Anastas, P. T.; Warner, J. C. *Green Chemistry: Theory and Practice*; Oxford University Press, 1998.
(31) Waldvogel, S. R.; Malkowsky, I. M.; Griesbach, U.; Pütter, H.; Fischer, A.; Hahn, M.; Kötz, R. Novel Fluorine-Free Electrolyte System for Supercapacitors. *Electrochem. Commun.* **2009**, *11*, 1237−1241.
(32) Fung, B. M.; Khitrin, A. K.; Ermolaev, K. An Improved Broadband Decoupling Sequence for Liquid Crystals and Solids. *J. Magn. Reson.* **2000**, *142*, 97−101.
(33) Sheldrick, G. M. A Short History of SHELX. *Acta Crystallogr., Sect. A: Found. Adv.* **2008**, *64*, 112−122.
(34) Sheldrick, G. M. SHELXT - Integrated Space-Group and Crystal-Structure Determination. *Acta Crystallogr., Sect. A: Found. Adv.* **2015**, *71*, 3−8.
(35) Dolomanov, O. V.; Bourhis, L. J.; Gildea, R. J.; Howard, J. A. K.; Puschmann, H. OLEX2: A Complete Structure Solution, Refinement and Analysis Program. *J. Appl. Crystallogr.* **2009**, *42*, 339−341.
(36) Shah, F. U.; Gnezdilov, O. I.; Khan, I. A.; Filippov, A.; Slad, N. A.; Johansson, P. Structural and Ion Dynamics in Fluorine-Free Oligoether Carboxylate Ionic Liquid-Based Electrolytes. *J. Phys. Chem. B* **2020**, *124*, 9690−9700.
(37) Timmermans, J. Plastic Crystals: A Historical Review. *J. Phys. Chem. Solids* **1961**, *18*, 1−8.
(38) MacFarlane, D. R.; Meakin, P.; Amini, N.; Forsyth, M. Structural Studies of Ambient Temperature Plastic Crystal Ion Conductors. *J. Phys.: Condens. Matter* **2001**, *13*, 8257.
(39) Das, S.; Saha, S.; Sahu, M.; Mondal, A.; Reddy, C. M. Temperature-Reliant Dynamic Properties and Elasto-Plastic to Plastic Crystal (Rotator) Phase Transition in a Metal Oxyacid Salt. *Angew. Chem., Int. Ed.* **2022**, *61*, No. e202115359.
(40) Wojnarowska, Z.; Cheng, S.; Yao, B.; Swadzba-Kwasny, M.; McLaughlin, S.; McGrogan, A.; Delavoux, Y.; Paluch, M. Pressure-Induced Liquid-Liquid Transition in a Family of Ionic Materials. *Nat. Commun.* **2022**, *13*, No. 1342.
(41) Guo, M.; Jayakumar, S.; Luo, M.; Kong, X.; Li, C.; Li, H.; Chen, J.; Yang, Q. The Promotion Effect of π-π Interactions in Pd NPs Catalysed Selective Hydrogenation. *Nat. Commun.* **2022**, *13*, No. 1770.
(42) Bai, W.; Chen, J.; Liu, F.; Zhang, J.; Zhang, X.; Gu, Z.; Yu, J. Effects of Aprotic Solvents on the Physicochemical Properties and Ferric Ion Oxidation Activity of Iron-Based Ionic Liquids. *Phys. Chem. Chem. Phys.* **2023**, *25*, 6295−6305.
(43) Kimura, K.; Motomatsu, J.; Tominaga, Y. Correlation between Solvation Structure and Ion-Conductive Behavior of Concentrated Poly(ethylene carbonate)-Based Electrolytes. *J. Phys. Chem. C* **2016**, *120*, 12385−12391.
(44) Shah, F. U.; Glavatskih, S.; Dean, P. M.; MacFarlane, D. R.; Forsyth, M.; Antzutkin, O. N. Halogen-Free Chelated Orthoborate Ionic Liquids and Organic Ionic Plastic Crystals. *J. Mater. Chem.* **2012**, *22*, 6928−6938.
(45) Forsyth, M.; Yoon, H.; Chen, F.; Zhu, H.; MacFarlane, D. R.; Armand, M.; Howlett, P. C. Novel Na^+ Ion Diffusion Mechanism in Mixed Organic−Inorganic Ionic Liquid Electrolyte Leading to High Na^+ Transference Number and Stable, High Rate Electrochemical Cycling of Sodium Cells. *J. Phys. Chem. C* **2016**, *120*, 4276−4286.

https://doi.org/10.1021/acs.cgd.4c01030
Cryst. Growth Des. 2024, 24, 8989−8998